

ACTION-BASED DYNAMICAL MODELLING OF THE MILKY WAY DISK WITH *ROADMAPPING* AND OUR IMPERFECT KNOWLEDGE OF THE “REAL WORLD”

WILMA H. TRICK^{1,2}, JO BOVY³, AND HANS-WALTER RIX¹

Draft version September 16, 2015

ABSTRACT

We present *RoadMapping*, a dynamical modelling machinery that aims to recover the Milky Way’s (MW) gravitational potential and the orbit distribution of stellar populations in the Galactic disk. *RoadMapping* is a full likelihood analysis that models the observed positions and velocities of stars with an equilibrium, three-integral distribution function (DF) in an axisymmetric potential. In preparation for the application to the large data sets of modern surveys like Gaia, we create and analyze a large suite of mock data sets and develop qualitative “rules of thumb” for which characteristics and limitations of data, model and machinery affect constraints on the potential and DF most. We find that, while the precision of the recovery increases with the number of stars, the numerical accuracy of the likelihood normalisation becomes increasingly important and dominates the computational efforts. The modelling has to account for the survey’s selection function, but *RoadMapping* seems to be very robust against small misjudgments of the data completeness. Large radial and vertical coverage of the survey volume gives in general the tightest constraints. But no observation volume of special shape or position and stellar population should be clearly preferred, as there seem to be no stars that are on manifestly more diagnostic orbits. We propose a simple approximation to include measurement errors at comparably low computational cost that works well if the distance error is $\lesssim 10\%$. The model parameter recovery is also still possible, if the proper motion errors are known to within 10% and are $\lesssim 2 \text{ mas yr}^{-1}$. We also investigate how small deviations of the stars’ distribution from the assumed DF influence the modelling: An over-abundance of high velocity stars affects the potential recovery more strongly than an under-estimation of the DF’s low-velocity domain. Selecting stellar populations according to mono-abundance bins of finite size can give reliable modelling results, as long as the DF parameters of two neighbouring bins do not vary more than 20% [TO DO: CKECK]. As the modelling has to assume a parametric form for the gravitational potential, deviations from the true potential have to be expected. We find, that in the axisymmetric case we can still hope to find a potential that is indeed a reliable best fit within the limitations of the assumed potential. Overall *RoadMapping* works as a reliable and unbiased estimator, and is robust against small deviations between model and the “real world”.

Keywords: Galaxy: disk — Galaxy: fundamental parameters — Galaxy: kinematics and dynamics — Galaxy: structure

1. INTRODUCTION

Stellar dynamical modelling can be employed to infer the Milky Way’s gravitational potential from the positions and motions of individual stars (Binney & Tremaine 2008; Binney 2011; Rix & Bovy 2013). Observational information on the 6D phase-space coordinates of stars is currently growing at a rapid pace, and will be taken to a whole new level in number and precision by the upcoming data from the Gaia mission (Perryman et al. 2001). Yet, rigorous and practical modelling tools that turn position-velocity data of individual stars into constraints both on the gravitational potential and on the distribution function (DF) of stellar orbits, are scarce (Rix & Bovy 2013) [TO DO: more references] [TO DO: References that explain that the modelling is scarce, or previous modelling approaches??] [TO DO: Hans-Walter suggested a Sanders & Binney ref-

erence, but I’m still not sure to what kind of paper: modelling approach or review of scarce modelling tools...]

The Galactic gravitational potential is fundamental for understanding the Milky Way’s dark matter and baryonic structure (Rix & Bovy 2013; McMillan 2012; Strigari 2013; Read 2014) and the stellar-population dependent orbit distribution function is a basic constraint on the Galaxy’s formation history (Binney 2013; Rix & Bovy 2013; Sanders & Binney 2015) [TO DO: more references].

There is a variety of practical approaches to dynamical modelling of discrete collisionless tracers, such as the stars in the Milky Way (e.g. Jeans modelling: Kuijken & Gilmore (1989), Bovy & Tremaine (2012), Garbari et al. (2012), Zhang et al. (2013), Büdenbender et al. (2015); action-based DF modelling: Bovy & Rix (2013), Piffl et al. (2014), Sanders & Binney (2015); torus modelling: McMillan & Binney (2012, 2013); Made-to-measure modelling: Syer & Tremaine (1996), De Lorenzi et al. (2007) or Hunt & Kawata (2014). Most of them – explicitly or implicitly – describe

Electronic address: trick@mpia.de

¹ Max-Planck-Institut für Astronomie, Königstuhl 17, D-69117 Heidelberg, Germany

² Correspondence should be addressed to trick@mpia.de.

³ University of Toronto [TO DO: What is Jo’s current address??]

the stellar distribution through a distribution function.

Actions are good ways to describe orbits, because they are canonical variables with their corresponding angles, have immediate physical meaning, and obey adiabatic invariance (McMillan & Binney 2008; Binney 2010; Binney & McMillan 2011; Binney 2011). Recently, Binney (2012) and Bovy & Rix (2013) [TO DO: are these the correct references??] proposed to combine parametrized axisymmetric potentials with DF's that are simple analytic functions of the three orbital actions to model discrete data. Binney (2010) and Binney & McMillan (2011) had proposed a set of simple action-based (quasi-isothermal) distribution functions (qDF). Ting et al. (2013) and Bovy & Rix (2013) showed that these qDF's may be good descriptions of the Galactic disk, when one only considers so-called mono-abundance populations (MAP), i.e. sub-sets of stars with similar $[\text{Fe}/\text{H}]$ and $[\alpha/\text{Fe}]$ (Bovy et al. 2012b,c,d).

Bovy & Rix (2013) implemented a rigorous modelling approach that put action-based DF modelling of the Galactic disk in an axisymmetric potential in practice. Given an assumed potential and an assumed DF, they directly calculated the likelihood of the observed (\vec{x}, \vec{v}) for each sub-set of MAP among SEGUE G-dwarf stars (Yanny et al. 2009). This modelling also accounted for the complex, but known selection function of the kinematic tracers. For each MAP, the modelling resulted in a constraint of its DF, and an independent constraint on the gravitational potential, which members of all MAPs feel the same way.

Taken as an ensemble, the individual MAP models constrained the disk surface mass density over a wide range of radii ($\sim 4 - 9$ kpc), and proved a powerful constraint on the disk mass scale length and on the disk-to-dark-matter ratio at the Solar radius.

Yet, these recent models still leave us poorly prepared with the wealth and quality of the existing and upcoming data sets. This is because Bovy & Rix (2013) made a number of quite severe and idealizing assumptions about the potential, the DF and the knowledge of observational effects (such as the selection function). All these idealizations are likely to translate into systematic error on the inferred potential or DF, well above the formal error bars of the upcoming data sets.

In this work we present *RoadMapping* ("Recovery of the Orbit Action Distribution of Mono-Abundance Populations and Potential INference for our Galaxy") - an improved and refined version of the original dynamical modelling machinery by Bovy & Rix (2013), making extensive use of the *galpy* Python package (Bovy 2015) and the *Stäckel Fudge* for fast action calculations by Binney (2012). *RoadMapping* is robust and well-tested and explicitly developed to exploit and deal with the large data sets of the future. *RoadMapping* explores and relaxes some of the restraining assumptions that Bovy & Rix (2013) made and is more flexible and more adept in dealing with large data sets. In this paper we set out to explore the robustness of *RoadMapping* against the breakdowns of some of the most important

assumptions of DF-based dynamical modelling. Our goal is to examine which aspects of the data, the model and the machinery itself limit our recovery of the true gravitational potential.

In the light of the imminent Gaia data, we analyze how well *RoadMapping* behaves in the limit of large data. For a huge number of stars three aspects become important, that may be hidden behind Poisson noise for smaller data sets: (i) We have to make sure that *RoadMapping* is an un-biased estimator (Section ??). (ii) Numerical inaccuracies in the actual modelling machinery must not be an important source of systematics (Section 2.6). (iii) As parameter estimates become so precise, we need more flexibility and more free parameters in the potential and DF model. The modelling machinery itself needs to be flexible and fast in effectively finding the best fit parameters for a large set of parameters. The improvements made to the machinery used in Bovy & Rix (2013) are presented in Section 2.7.

We also explore how different aspects of the observational experiment design impact the parameter recovery. (i) In an era where we can choose data from different MW surveys, it might be worth to explore if different regions within the MW (i.e. differently shaped or positioned survey volumes) are especially diagnostic to recover the potential (Section ??). (ii) What happens if our knowledge about the selection function, specifically the completeness of the data set within the survey volume, is systematically imperfect (Section ??)? (iii) How to best account for individual measurement errors in the modelling (Section ??)?

One of the strongest assumptions is to restrict the dynamical modelling to a certain family of parametrized models. We investigate how well we can hope to recover the true potential, when our potential and DF models do not encompass the true potential and DF. First, we examine in Section ?? what would happen if the stars within MAPs do intrinsically not follow a single qDF as assumed by Ting et al. (2013) and Bovy & Rix (2013). Second, we test in Section ?? how well the modelling works, if our assumed potential family deviates from the true potential.

The strongest assumption that goes into this kind of dynamical modelling might be the idealization of the Galaxy to be axi-symmetric and being in steady state. We do not investigate this within the scope of this paper but strongly suggest a systematic investigation of this for future work.

For all of the above aspects we show some plausible and illustrative examples on the basis of investigating mock data. The mock data is generated from galaxy models presented in Sections 2.1-2.4 following the procedure in Section 2.5, analysed according to the description of the machinery in Section 2.6-2.7 and the results are presented in Section 3 and discussed in Section ??.

[TO DO: Comment from Hans-Walter: Make sure, any topic/issue appears only once] [TO DO: Is now one quarter shorter than before. But maybe shorten it even

more...] [TO DO: Comment from Hans-Walter: Make clear "new in this paper", "general background", "exactly as in BR13"]

2. DYNAMICAL MODELLING

[TO DO: HW: In this section you have to indicate somehow, where you recapitulate BR13 and what is added new. "as in BR13", "beyond BR13"]

In this section we summarize the basic elements of *RoadMapping*, the dynamical modelling machinery presented in this work, which in many respects follows Bovy & Rix (2013).

2.1. Coordinate System

Our modelling takes place in the Galactocentric rest-frame with cylindrical coordinates $\mathbf{x} \equiv (R, \phi, z)$ and corresponding velocity components $\mathbf{v} \equiv (v_R, v_\phi, v_z)$. If the stellar phase-space data is given in observed heliocentric coordinates, position $\hat{\mathbf{x}} \equiv (\text{RA}, \text{DEC}, m - M)$ in right ascension RA, declination DEC and distance modulus $(m - M)$ as proxy for the distance from the sun, and velocity $\hat{\mathbf{v}} \equiv (\mu_{\text{RA}}, \mu_{\text{DEC}}, v_{\text{los}})$ as proper motions $\boldsymbol{\mu} = (\mu_{\text{RA}}, \mu_{\text{DEC}})$ [TO DO: cos somewhere??] in both RA and DEC direction and line-of-sight velocity v_{los} , the data $(\hat{\mathbf{x}}, \hat{\mathbf{v}})$ has to be converted first into the Galactocentric rest-frame coordinates (\mathbf{x}, \mathbf{v}) using the sun's position and velocity. We assume for the sun

$$\begin{aligned} (R_\odot, \phi_\odot, z_\odot) &= (8 \text{ kpc}, 0^\circ, 0 \text{ kpc}) \\ (v_{R,\odot}, v_{T,\odot}, v_{z,\odot}) &= (0, 230, 0) \text{ km s}^{-1}. \end{aligned}$$

2.2. Actions and Potential Models

Orbits in axisymmetric potentials are best described and fully specified by the three actions $\mathbf{J} \equiv (J_R, J_z, J_\phi = L_z)$, defined as

$$J_i = \frac{1}{2\pi} \oint_{\text{orbit}} p_i dx_i, \quad (1)$$

and which depend on the potential via the connection between position x_i and momentum p_i along the orbit. Actions have a clear physical meaning: They quantify the amount of oscillation in each coordinate direction of the full orbit [TO DO: REF: HW suggested Binney & Tremaine (2008), but I can't find a corresponding statement in the book]. The position of a star along the orbit is denoted by a set of angles, which form together with the angles a set of canonical conjugate phase-space coordinates (Binney & Tremaine 2008, §3.5.1).

Even though actions are excellent orbit labels and arguments for stellar distribution functions, their computation is typically very expensive and depends on the choice of potential in which the star moves. The spherical isochrone potential (Hénon 1959) is the only [TO DO: Jo suggested "most general Galactic" instead of "only", but the isochrone is actually not Galactic... Ask him.] potential for which Equation 1 takes an analytic form (Binney & Tremaine 2008, §3.5.2). For Stäckel potentials actions can be calculated exactly by the (numerical) evaluation of a single integral. In all other potentials numerically calculated actions will always be approximations, unless Equation 1 is integrated along

the whole (often not periodic) orbit. A computational fast way to get actions for arbitrary axisymmetric potentials is the *Stäckel fudge* by Binney (2012), which locally approximates the potential by a Stäckel potential. To speed up the calculation even more, an interpolation grid for J_R and J_z in energy E , angular momentum L_z and [TO DO: what else??] can be build out of these Stäckel fudge actions, as described in Bovy (2015).⁴

For the gravitational potential in our modelling we assume a family of parametrized potential models with a fixed number of free parameters. We use different kinds of potentials: The Milky Way like potential from Bovy & Rix (2013) (MW13-Pot) with bulge, disk and halo; the spherical isochrone potential (Iso-Pot) in our test suites to make use of the analytic (and therefore exact and fast) way to calculate actions; and the 2-component Kuzmin-Kutuzov Stäckel potential (Batsleer & Dejonghe 1994; KKS-Pot), which displays a disk and halo structure and also provides exact actions. Table ?? summarizes all reference potentials together used in this work with their free parameters p_Φ . The density distribution of these potentials is illustrated in Figure 1.

2.3. Stellar Distribution Functions

Throughout, we assume that the orbits of each MAP can be described by a single qDF of the form given by Binney & McMillan (2011). This is motivated by the findings of Bovy et al. (2012b,c,d) and Ting et al. (2013) about the simple phase-space structure of MAPs, and following Bovy & Rix (2013) and their successful application. This qDF has the form

$$\begin{aligned} \text{qDF}(\mathbf{J} | p_{\text{DF}}) \\ = f_{\sigma_R}(J_R, L_z | p_{\text{DF}}) \times f_{\sigma_z}(J_z, L_z | p_{\text{DF}}) \end{aligned} \quad (2)$$

with

$$\begin{aligned} f_{\sigma_R}(J_R, L_z | p_{\text{DF}}) &= n \times \frac{\Omega}{\pi \sigma_R^2(R_g) \kappa} \exp\left(-\frac{\kappa J_R}{\sigma_R^2(R_g)}\right) \\ &\times [1 + \tanh(L_z/L_0)] \end{aligned} \quad (3)$$

$$f_{\sigma_z}(J_z, L_z | p_{\text{DF}}) = \frac{\nu}{2\pi \sigma_z^2(R_g)} \exp\left(-\frac{\nu J_z}{\sigma_z^2(R_g)}\right). \quad (4)$$

Here $R_g \equiv R_g(L_z)$ and $\Omega \equiv \Omega(L_z)$ are the (guiding-center) radius and the circular frequency of the circular orbit with angular momentum L_z in a given potential. $\kappa \equiv \kappa(L_z)$ and $\nu \equiv \nu(L_z)$ are the radial/epicycle (κ) and vertical (ν) frequencies with which the star would oscillate around the circular orbit in R - and z -direction when slightly perturbed (Binney & Tremaine 2008, §3.2.3) [TO DO: ask someone, if I'm messing up different definitions of κ]. The term $[1 + \tanh(L_z/L_0)]$ suppresses counter-rotation for orbits in the disk with $L \gg L_0$ which we set to a small value ($L_0 = 10 \times R_\odot/8 \times v_{\text{circ}}(R_\odot)/220$ [TO DO: Jo said, galpy default is 10 km/s kpc. But I got the value actually from the code...]). To match the observed properties of MAPs (see

⁴ [TO DO: Write which numerical accuracy I needed for the grid, as the default values were not good enough.]

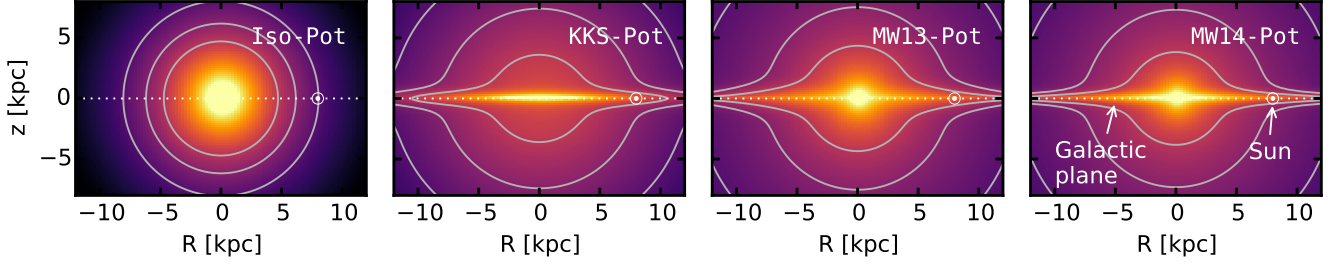


Figure 1. Density distribution of the four reference galaxy potentials in Table ??, for illustration purposes. These potentials are used throughout this work for mock data creation and potential recovery. [TO DO: Potential and/or population names in typewriter]

Bovy et al. 2012b,c,d), we chose the functional forms

$$n(R_g | p_{\text{DF}}) \propto \exp\left(-\frac{R_g}{h_R}\right) \quad (5)$$

$$\sigma_R(R_g | p_{\text{DF}}) = \sigma_{R,0} \times \exp\left(-\frac{R_g - R_\odot}{h_{\sigma,R}}\right) \quad (6)$$

$$\sigma_z(R_g | p_{\text{DF}}) = \sigma_{z,0} \times \exp\left(-\frac{R_g - R_\odot}{h_{\sigma,z}}\right), \quad (7)$$

which indirectly set the stellar number density and radial and vertical velocity dispersion profiles. The qDF for each MAP has therefore a set of five free parameters p_{DF} : the density scale length of the tracers h_R , the radial and vertical velocity dispersion at the solar position R_\odot , $\sigma_{R,0}$ and $\sigma_{z,0}$, and the scale lengths $h_{\sigma,R}$ and $h_{\sigma,z}$, that describe the radial decrease of the velocity dispersion. Throughout this work we use for illustration purposes a few example stellar populations, each following a single qDF, whose parameters are given in Table ?. Most tests use the `hot` and `cool` qDFs from Table ?, which correspond to kinematically hot and cool populations, respectively.

One crucial point in our dynamical modelling technique (§2.6), as well as in creating mock data (§2.5), is to calculate the (axisymmetric) spatial tracer density $\rho_{\text{DF}}(\mathbf{x} | p_\Phi, p_{\text{DF}})$ for a given qDF and potential. We do this by integrating the qDF at a given (R, z) over all three velocity components, using a N_v -th order Gauss-Legendre quadrature for each integral:

$$\rho_{\text{DF}}(R, |z| | p_\Phi, p_{\text{DF}}) = \int_{-\infty}^{\infty} \text{qDF}(\mathbf{J}[R, z, \mathbf{v} | p_\Phi] | p_{\text{DF}}) d^3\mathbf{v} \quad (8)$$

$$\approx \int_{-n_\sigma \sigma_R(R | p_{\text{DF}})}^{n_\sigma \sigma_R(R | p_{\text{DF}})} \int_{-n_\sigma \sigma_z(R | p_{\text{DF}})}^{n_\sigma \sigma_z(R | p_{\text{DF}})} \int_0^{1.5v_{\text{circ}}(R_\odot)} \text{qDF}(\mathbf{J}[R, z, \mathbf{v} | p_\Phi] | p_{\text{DF}}) dv_T dv_z dv_R, \quad (9)$$

where $\sigma_R(R | p_{\text{DF}})$ and $\sigma_z(R | p_{\text{DF}})$ are given by Equations 6 and 7 and the integration ranges are motivated by Figure 2. The integration range $[0, 1.5v_{\text{circ}}(R_\odot)]$ over v_T is in general sufficient (only for observation volumes at smaller Galactocentric radii with larger velocities this upper limit needs to be increased). For a given p_Φ and p_{DF} we explicitly calculate the density on $N_x \times N_x$ regular grid points in the (R, z) plane; in between grid points the density is evaluated with a bivariate spline interpolation.

The grid is chosen to cover the extent of the observations (for $|z| \leq 0$, because the model is symmetric in z by construction). The total number of actions that need to be calculated to set up the density interpolation grid is $N_x^2 \cdot N_v^3$. §2.6 and Figure ?? show the importance of choosing N_x , N_v and n_σ sufficiently large in order to get the density with an acceptable numerical accuracy [TO DO: Jo thinks that this statement is difficult to understand here, because you have not yet talked about the normalization].

2.4. Selection Functions

Any survey's selection function can be understood as defining an effective sample subvolume in the space of observables: e.g. position on the plane of the sky (the survey area), distance from the sun (limited by the brightness of the stars and the sensitivity of the detector), colors and metallicity of the stars (limited by survey mode and targeting).

We simply use spatial selection functions, which describe the probability to observe a star at \mathbf{x} ,

$$\text{sf}(\mathbf{x}) \equiv \begin{cases} \text{completeness}(\mathbf{x}) & \text{if } \mathbf{x} \text{ within observed volume} \\ 0 & \text{outside.} \end{cases}$$

For the observed volume we use simple geometrical shapes. Either a sphere of radius r_{max} with the sun at its center, or an angular segment of an cylindrical annulus (`wedge`), i.e. the volume with $R \in [R_{\text{min}}, R_{\text{max}}]$, $\phi \in [\phi_{\text{min}}, \phi_{\text{max}}]$, $z \in [z_{\text{min}}, z_{\text{max}}]$ within the model galaxy. The sharp outer cut of the survey volume could be understood as the detection limit in apparent brightness in the case, where all stars have the same luminosity. Here $0 \leq \text{completeness}(\mathbf{x}) \leq 1$ everywhere inside the observed volume, so it can be understood as a position-dependent detection probability. Unless explicitly stated otherwise, we simplify to $\text{completeness}(\mathbf{x}) = 1$.

2.5. Mock Data

We will rely on mock data as input to explore the limitations of the modelling. We investigate this, we assume first that our measured stars do indeed come from our assumed families of potentials and distribution functions and draw mock data from a given true distribution. Subsequently, we manipulate and modify these mock data sets to mimic observational effects.

The distribution function is given in terms of actions and angles. The transformation $(\mathbf{J}_i, \boldsymbol{\theta}_i) \rightarrow (\mathbf{x}_i, \mathbf{v}_i)$ is however difficult to perform and computationally much more

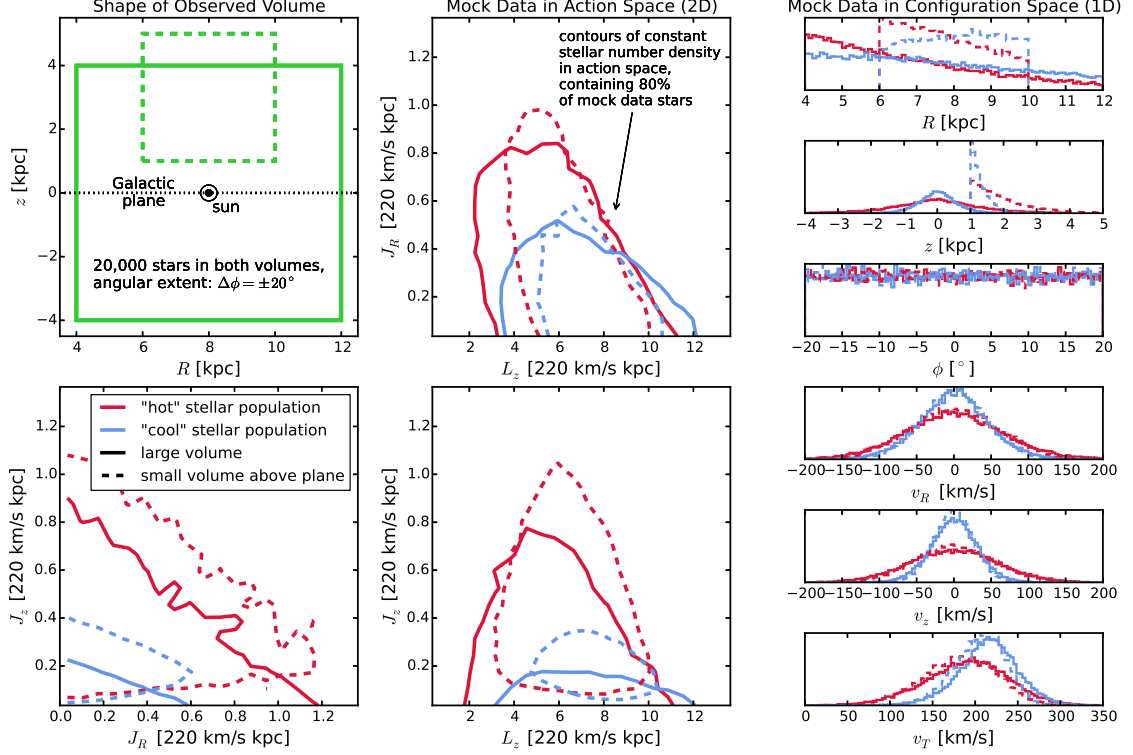


Figure 2. Distribution of mock data in action space (2D iso-density contours, enclosing 80% of the stars, the two central and the lower left panel) and configuration space (1D histograms, right panels), depending on shape and position of the survey observation volume and temperature of the stellar population. The parameters of the mock data model is given as Test ?? in Table ?. In the upper left panel we demonstrate the shape of the two different wedge-like observation volumes within which we were creating each a hot (red) and cool (blue) mock data set: a large volume centred on the Galactic plane (solid lines) and a smaller one above the plane (dashed lines). The distribution in action space visualizes how orbits with different actions also reach into different regions within the Galaxy. The 1D histograms on the right illustrate that qDFs generate realistic stellar distributions in galactocentric coordinates $(R, z, \phi, v_R, v_z, v_T)$. [TO DO: fancybox Legend] [TO DO: Potential and/or population names in typewriter font] [TO DO: Jo suggests to make two or three separate figures out of this. I'm not yet convinced, as I think it is nice and tidy like this.]

expensive than the transformation $(\mathbf{x}_i, \mathbf{v}_i) \rightarrow (\mathbf{J}_i, \boldsymbol{\theta}_i)$. We employ a fast and simple two-step method for drawing mock data from an action distribution function, which also accounts effectively for a given survey selection function.

In the first step we draw positions \mathbf{x}_i for our mock data stars from the selection function and tracer density. We start by setting up the interpolation grid for the tracer density $\rho(R, |z| | p_\Phi, p_{\text{DF}})$ generated by the given qDF and according to §2.3 and Equation 9. For the creation of the mock data we use $N_x = 20$, $N_v = 40$ and $n_\sigma = 5$. Next, we sample random positions (R_i, z_i, ϕ_i) uniformly within the entire observable volume. Then we apply a rejection Monte Carlo method to these positions using the pre-calculated $\rho_{\text{DF}}(R, |z| | p_\Phi, p_{\text{DF}})$. To apply a non-uniform selection function, $\text{sf}(\mathbf{x}) \neq \text{const.}$ within the observed volume, we use the rejection method a second time. The resulting sample then follows $\mathbf{x}_i \rightarrow p(\mathbf{x}) \propto \rho_{\text{DF}}(R, |z| | p_\Phi, p_{\text{DF}}) \times \text{sf}(\mathbf{x})$.

In the second step we draw velocities according to the distribution function. The velocities are independent of the selection function within the observed volume. For each of the positions (R_i, z_i) we sample velocities directly from the qDF $(R_i, z_i, \mathbf{v} | p_\Phi, p_{\text{DF}})$ using a rejection method. To reduce the number of rejected velocities, we use a Gaussian in velocity space as an envelope function,

from which we first randomly sample velocities and then apply the rejection method to shape the Gaussian velocity distribution towards the velocity distribution predicted by the qDF. We now have a mock data satisfying $(\mathbf{x}_i, \mathbf{v}_i) \rightarrow p(\mathbf{x}, \mathbf{v}) \propto \text{qDF}(\mathbf{x}, \mathbf{v} | p_\Phi, p_{\text{DF}}) \times \text{sf}(\mathbf{x})$.

Figure 2 shows examples of mock data sets in configuration space (\mathbf{x}, \mathbf{v}) and action space. The mock data from the qDF lead to the expected distributions in configuration space: More stars are found at smaller R and $|z|$, and are distributed uniformly in ϕ according to our assumption of axisymmetry. The distribution in radial and vertical velocities, v_R and v_z , is approximately Gaussian with the (total projected) velocity dispersion being $\sim \sigma_{R,0}$ and $\sim \sigma_{z,0}$ (see Table ?). The distribution of tangential velocities v_T is skewed because of asymmetric drift. The distribution in action space illustrates the intuitive physical meaning of actions: The stars of the cool population have in general lower radial and vertical actions, as they are on more circular orbits. The different relative distributions of the radial and vertical actions J_R and J_z of the hot and cool population is due to them having different velocity anisotropy $\sigma_{R,0}/\sigma_{z,0}$. The different ranges of angular momentum L_z in the two volumes reflect $L_z \sim Rv_{\text{circ}}$ and the different radial extent of both volumes. The volume above the plane contains stars with higher J_z , because stars with small J_z cannot reach that far above the

plane. Circular orbits with $J_R = 0$ and $J_z = 0$ can only be observed in the Galactic mid-plane. An orbit with L_z much smaller or larger than $L_z(R_\odot)$ can only reach into a volume located around R_\odot , if it is more eccentric and has therefore larger J_R . This together with the effect of asymmetric drift can be seen in the asymmetric distribution of J_R in the top central panel of Figure 2.

If we want to add measurement errors to the mock data, we need to apply the following modifications to the above procedure. First, measurement errors are best described in heliocentric observables (see Section 2.1), we therefore assume and apply Gaussian errors to the *true* phase-space coordinates $\tilde{\mathbf{x}} = (\text{RA}, \text{DEC}, (m - M))$, $\tilde{\mathbf{v}} = (\mu_{\text{RA}}, \mu_{\text{DEC}}, v_{\text{los}})$, where we have taken $(m - M)$ as a proxy for distance. Second, in the case of distance errors, stars can virtually scatter in and out of the observed volume. To account for this, we draw the *true* positions from a volume that is larger than the actual observation volume, perturb the stars positions according to the distance errors and then reject all stars that lie now outside of the observed volume. This procedure mirrors the Poisson scatter around the detection threshold for stars whose distances are determined from the apparent brightness and the distance modulus. We then sample velocities (given the *true* positions of the stars) as described above and perturb them according to the measurement errors as well.

2.6. Data Likelihood

As data we consider here the positions and velocities of stars coming from a given MAP and survey selection function $\text{sf}(\mathbf{x})$,

$$D = \{\mathbf{x}_i, \mathbf{v}_i \mid (\text{star } i \text{ belonging to same MAP}) \wedge (\text{sf}(\mathbf{x}_i) > 0)\}.$$

The model that we fit is specified by a number of fixed and free parameters,

$$p_M = \{p_{\text{DF}}, p_\Phi\}.$$

As qDF parameters (see Section 2.3) we use

$$p_{\text{DF}} := \{ \ln(h_R/8\text{kpc}), \ln(\sigma_{R,0}/220\text{km s}^{-1}), \ln(\sigma_{z,0}/220\text{km s}^{-1}), \ln(h_{\sigma,R}/8\text{kpc}), \ln(h_{\sigma,z}/8\text{kpc}) \}. \quad (10)$$

The orbit of the i -th star in a potential with p_Φ is labeled by the actions $\mathbf{J}_i := \mathbf{J}[\mathbf{x}_i, \mathbf{v}_i \mid p_\Phi]$ and the qDF evaluated for the i -th star is then $\text{qDF}(\mathbf{J}_i \mid p_M) := \text{qDF}(\mathbf{J}[\mathbf{x}_i, \mathbf{v}_i \mid p_\Phi] \mid p_{\text{DF}})$.

The likelihood of the data given the model $\mathcal{L} = (D \mid p_M)$ is the product of the probabilities for each star to move in the potential with p_Φ , being within the survey's selection function and it's orbit to be drawn from the

qDF with p_{DF} , i.e.

$$\begin{aligned} \mathcal{L}(D \mid p_M) &\equiv \prod_i^N p(\mathbf{x}_i, \mathbf{v}_i \mid p_M) \\ &= \prod_i^N \frac{\text{qDF}(\mathbf{J}_i \mid p_M) \cdot \text{sf}(\mathbf{x}_i)}{\int d^3x d^3v \text{qDF}(\mathbf{J} \mid p_M) \cdot \text{sf}(\mathbf{x})} \\ &\propto \prod_i^N \frac{\text{qDF}(\mathbf{J}_i \mid p_M)}{\int d^3x \rho_{\text{DF}}(R, |z| \mid p_M) \cdot \text{sf}(\mathbf{x})}, \end{aligned} \quad (11)$$

where N is the number of stars in the data set D , and in the last step we used Equation 8. The factor $\prod_i \text{sf}(\mathbf{x}_i)$ is independent of the model parameters, so we simply evaluate Equation 11 in the likelihood calculation. We find the best set of model parameters by maximizing the posterior probability distribution $\text{pdf}(p_M \mid D)$, which is according to Bayes' theorem proportional the likelihood $\mathcal{L}(D \mid p_M)$ times the prior. We assume flat priors in both p_Φ and p_{DF} (see Equation 10) throughout this work, then pdf and likelihood can be used interchangeably.

The normalisation in Equation 11 is a measure for the total number of tracers inside the survey volume,

$$M_{\text{tot}} \equiv \int d^3x \rho_{\text{DF}}(R, |z| \mid p_M) \cdot \text{sf}(\mathbf{x}). \quad (12)$$

In the case of an axisymmetric galaxy model and $\text{sf}(\mathbf{x}) = 1$ everywhere inside the observed volume (i.e. a complete sample as assumed in most tests in this work), the normalisation is essentially a two-dimensional integral in R and z of the interpolated tracer density ρ_{DF} in Equation 9 over the differential survey volume, i.e. $\frac{\partial M_{\text{tot}}}{\partial \phi}(R, z) = \int dR dz \rho_{\text{DF}} \times \frac{\partial V}{\partial \phi}$ [TO DO: missing factor of R ???]. We perform this integral as a Gauss Legendre quadrature of order 40 in each R and z direction. The angular integral, i.e. $M_{\text{tot}} = \int R d\phi \frac{\partial M_{\text{tot}}}{\partial \phi}$, can be solved analytically.

It turns out that the sufficiently accurate evaluation of the likelihood is computationally expensive, even for only one set of model parameters. This expense is dominated by the number of action calculations required, which in turn depends on the number of stars in the sample and the numerical accuracy of the integrals in Equation 9 needed for the normalisation, which requires $N_x^2 \times N_v^3$ action calculations. The accuracy has to be chosen high enough, such that a resulting numerical error

$$\begin{aligned} \delta_{M_{\text{tot}}} &\equiv \frac{M_{\text{tot,approx}}(N_x, N_v, N_\sigma) - M_{\text{tot}}}{M_{\text{tot}}} \end{aligned} \quad (13)$$

[TO DO: make sure every $M_{\text{tot,true}}$ is replaced by M_{tot}] does not dominate the likelihood, i.e.

$$\begin{aligned} \log \mathcal{L}(p_M \mid D) &= \sum_i^N \log \text{qDF}(\mathbf{J}_i \mid p_M) - 3N \log(r_o v_o) \\ &\quad - N \log(M_{\text{tot}}) - N \log(1 + \delta_{M_{\text{tot}}}), \end{aligned} \quad (14)$$

with

$$N \log(1 + \delta_{M_{tot}}) \lesssim 1.$$

In other words, this error is only small enough, if it does not affect the comparison of two adjacent models whose likelihoods differ, to be clearly distinguishable, by a factor of 10. Otherwise numerical inaccuracies could lead to systematic biases in the potential and DF fitting. For data sets as large as $N = 20,000$ stars in one MAP, which in the age of Gaia could very well be the case [TO DO: Really???], we would need a numerical accuracy of 0.005% in the normalisation. Figure ?? demonstrates that the numerical accuracy we use in the analysis, $N_x = 16$, $N_v = 24$ and $N_{sigma} = 5$, does satisfy this requirement.

If the data is affected by measurement errors, they have to be accounted for in the likelihood. We assume Gaussian errors in the observable space $\mathbf{y} \equiv (\tilde{\mathbf{x}}, \tilde{\mathbf{v}}) = (\text{RA}, \text{DEC}, (m - M), \mu_{\text{RA}}, \mu_{\text{DEC}}, v_{\text{los}})$,

$$N[\mathbf{y}_i, \delta \mathbf{y}_i](\mathbf{y}') = N[\mathbf{y}', \delta \mathbf{y}_i](\mathbf{y}_i) \\ \equiv \prod_k \frac{1}{\sqrt{2\pi}(\delta y_{i,k})^2} \exp\left(-\frac{(y_{i,k} - y'_{i,k})^2}{2(\delta y_{i,k})^2}\right),$$

where $y_{i,k}$ is the k -th coordinate in \mathbf{y}_i of the i -th star. Observed stars follow the (quasi-isothermal) distribution function ($\text{DF}(\mathbf{y}) \equiv \text{qDF}(\mathbf{J}[\mathbf{y} | p_\Phi] | p_{\text{DF}})$ for short), convolved with the error distribution $N[0, \delta \mathbf{y}](\mathbf{y})$. The selection function $\text{sf}(\mathbf{y})$ acts on the space of (error affected) observables. Then the probability of one star coming from potential p_Φ , distribution function p_{DF} and being affected by the measurement errors $\delta \mathbf{y}$ becomes

$$\tilde{p}(\mathbf{y}_i | p_\Phi, p_{\text{DF}}, \delta \mathbf{y}_i) \\ \equiv \frac{\text{sf}(\mathbf{y}_i) \cdot \int d^6 \mathbf{y}' \text{DF}(\mathbf{y}') \cdot N[\mathbf{y}_i, \delta \mathbf{y}_i](\mathbf{y}')}{\int d^6 \mathbf{y} \text{DF}(\mathbf{y}) \cdot \int d^6 \mathbf{y}' \text{sf}(\mathbf{y}') \cdot N[\mathbf{y}, \delta \mathbf{y}_i](\mathbf{y}')}.$$

In the case of errors in distance or position, the evaluation of this is computational expensive - especially if the stars' have heteroscedastic errors $\delta \mathbf{y}_i$, for which the normalisation would have to be calculated for each star separately. In practice we apply the following approximation:

$$\tilde{p}(\mathbf{y}_i | p_\Phi, p_{\text{DF}}, \delta \mathbf{y}_i) \\ \approx \frac{\text{sf}(\mathbf{x}_i)}{\int d^6 \mathbf{y} \text{DF}(\mathbf{y}) \cdot \text{sf}(\mathbf{x})} \cdot \frac{1}{N_{\text{error}}} \sum_n^{N_{\text{error}}} \text{DF}(\mathbf{x}_i, \mathbf{v}[\mathbf{y}'_{i,n}]) \quad (15)$$

with

$$\mathbf{y}'_{i,n} \sim N[\mathbf{y}_i, \delta \mathbf{y}_i](\mathbf{y}')$$

In doing so, we ignore errors in the star's position \mathbf{x}_i [TO DO: something is not clear to HW here] altogether. This simplifies the normalisation drastically and makes it independent of measurement errors, including the velocity errors. Distance errors however are included [TO DO: something is not clear to HW here], but only implicitly in the convolution over the stars' velocity errors in the Galactocentric rest frame. We calculate the convolution using Monte Carlo integration with N_{error} samples drawn from the full error Gaussian in

observable space, $\mathbf{y}'_{i,n}$.

2.7. Fitting Procedure

To search the (p_Φ, p_{DF}) parameter space for the maximum of the likelihood in Equation 11, we go beyond the fixed grid search by Bovy & Rix (2013) and employ an effective two-step procedure: The first step finds the approximate peak and width of the likelihood using a nested-grid search, while the second step samples the shape of the likelihood using a Monte-Carlo Markov Chain (MCMC) approach.

Fitting Step 1: Nested-grid search.— The (p_Φ, p_{DF}) parameter space can be high-dimensional. To effectively minimizing the number of likelihood evaluations before finding its peak, we use a nested-grid approach:

- *Initialization.* For N free model parameters $M = (p_\Phi, p_{\text{DF}})$, we set up a sufficiently large initial grid with 3^N regular grid points.
- *Evaluation.* We evaluate the likelihood at each grid-point similar to Bovy & Rix (2013) (their Figure 9): Because of the many computationally expensive $\mathbf{x}, \mathbf{v} \xrightarrow{p_\Phi} \mathbf{J}$ transformations that have to be performed for each new set of p_Φ parameters, an outer loop iterates over the p_Φ parameters and precalculates the actions, while an inner loop evaluates the likelihood Equation 11 for all qDF parameters p_{DF} with the actions in the given potential.
- *Iteration.* To find from the very sparse 3^N likelihood grid a new grid, that is more centered on the likelihood and has a width of order of the width of the likelihood, we proceed as follows: For each of the model parameter in M we marginalize the likelihood by summing over the grid. If the resulting 3 points all lie within 4σ of a Gaussian, we fit a Gaussian to the 3 points and determine a new 4σ fitting range. Otherwise the boundaries of the grid point with the highest likelihood becomes the new fitting range. We proceed with iteratively evaluating the likelihood on finer and finer grids, until we have found a 4-sigma fit range in each of the model parameter dimensions.
- *The fiducial qDF.* For the above strategy to work properly, the action pre-calculations have to be independent of the choice of qDF parameters. This is clearly the case for the $N_j \times N_{\text{error}}$ stellar data actions \mathbf{J}_i . To calculate the normalisation in Equation 11, $N_x^2 \times N_v^3$ actions \mathbf{J}_n are needed. Formally the spatial coordinates at which the \mathbf{J}_n are calculated depend on the p_{DF} parameters via the integration ranges in Equation 9. To relax this dependence we instead use the same velocity integration limits in the likelihood calculations for all p_{DF} s in a given potential. This set of parameters, that sets the velocity integration range globally, $(\sigma_{R,0}, \sigma_{z,0}, h_{\sigma,R}, h_{\sigma,z})$ in Equation 6 and 7, is referred to as the *fiducial* qDF. Using the same integration range in the density calculation for all qDFs at a given p_Φ makes the normalisation vary smoothly with different p_{DF} . Choosing a fiducial

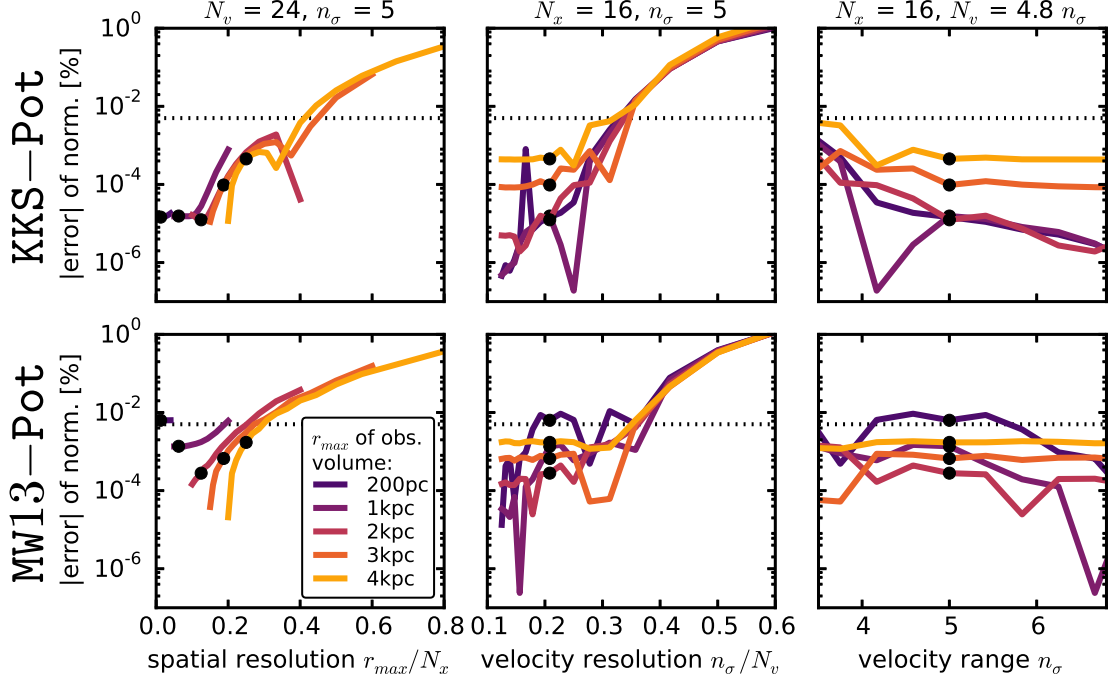


Figure 3. Relative error δM_{tot} of the likelihood normalization M_{tot} in Equation 13 depending on the accuracy of the grid-based density calculation in Equation 9 (and surrounding text). We show how δM_{tot} varies with the spatial resolution (first column), velocity resolution (second column) and velocity integration range (third column) for two different potentials (KKS-Pot in the first row and MW13-Pot in the second row) and five different spherical observation volumes with radius r_{max} (color coded according to the legend). (Test ?? in Table ?? summarizes all model parameters.) N_x is the number of spatial grid points in $R \in R_{\odot} \text{ kpc} \pm r_{\text{max}}$ and $|z| \in [0, r_{\text{max}}]$ on which the density is evaluated according to Equation 9. The spatial resolution in z is therefore r_{max}/N_x and $2r_{\text{max}}/N_x$ in R . This choice is reasonable because the density is symmetric in z and varies less in R than in z , because the tracer scale length of the disk is much larger than its scale height. At each (R, z) of the grid a Gauss-Legendre integration of order N_v is performed over an integration range of $\pm n_{\sigma}$ times the velocity dispersion in v_R and v_z and $[0, 1.5v_{\text{circ}}(R_{\odot})]$ in v_T . n_{σ}/N_v is therefore a proxy for the velocity resolution of the grid. (We vary N_x , N_v and n_{σ} separately and keep the other two fixed at the values indicated above the columns.) To arrive at the approximation $M_{\text{tot,approx}}$ for M_{tot} in Equation 12, we perform a 40th-order Gauss-Legendre integration in each R and z direction of the interpolated density over the observed volume. We calculate the “true” normalization with high accuracy as $M_{\text{tot}} \approx M_{\text{tot,approx}}(N_x = 20, N_v = 56, N_{\sigma} = 7)$. The black dots indicate the accuracy used in our analyses: It is better than 0.002%. Only for the smallest volume in the MW13-Pot (yellow line) the error is only $\sim 0.005\%$. This could be due to the fact, that, while we have analytical formulas to calculate the actions for the Staechel potential KKS-Pot exactly, we have to resort to an approximate action calculation for the MW-like potential MW13-Pot (see Section 2.2). [TO DO: Write $|\delta M_{\text{tot}}|$ on y-axis]

qDF that is very different from the true qDF can however lead to large biases. The optimal values for the fiducial qDF are the (yet unknown) best fit p_{DF} parameters. We take care of this by setting, in each iteration step of the nested-grid search, the fiducial qDF simply to the p_{DF} parameters of the central grid point. As the nested-grid search approaches the best fit values, the fiducial qDF approaches automatically the optimal values as well. This is another advantage of the nested-grid search, because the result will not be biased by a poor choice of the fiducial qDF.

- *Speed Limitations.* Overall the computation speed of this nested-grid approach is dominated (in descending order of importance) by a) the complexity of potential and action calculation, b) the number $N_j \times N_{\text{error}} + N_x^2 \times N_v^3$ of actions to calculate, i.e. the number of stars, error samples and numerical accuracy of the normalisation calculations, c) the number of different potentials to investigate (i.e. the number of free potential parameters and number of grid points in each dimension) and d) the number of qDFs to investigate. The latter is also non-negligible, because for such a large number

of actions the number of qDF-function evaluations also take some time.

Fitting Step 2: MCMC. — After the nested-grid search is converged, the grid is centered at the peak of the likelihood and its extent contains the 4σ confidence interval. To actually sample the full shape of the likelihood, we could do a grid search with much finer grid spacing (e.g. $K = 11$ in each dimension). The number of grid points scales as a power of the free parameters N . For a large number of free parameters ($N > 4$) a Monte Carlo Markov Chain (MCMC) approach might sample the likelihood (with is here equivalent to the *pdf*, see §2.6) much faster. We use *emcee* by Foreman-Mackey et al. (2013) and release the walkers very close to the likelihood peak found by the nested-grid search, which will assure fast convergence in much less than K^N likelihood evaluations. For a sufficiently high numerical accuracy in calculating the integrals in Equation 9 the current qDF at each walker position can be used as the fiducial qDF. To get reasonable results also for slightly lower accuracy, a single fiducial qDF can be used for all likelihood evaluations within the MCMC as well. As fiducial qDF we use the qDF parameters of the likelihood peak, found by the nested-grid search.

3. RESULTS

We are now in a position to explore the questions about the ultimate limitations of action based modelling, posed in the introduction:

- Can we still retrieve unbiased model parameter estimates p_M in the limit of large sample sizes?
- What role does the survey volume and geometry play, at given sample size?
- What if our knowledge of the sample selection function is imperfect, and potentially biased?
- How do the parameter estimates deteriorate if the individual errors on the phase-space coordinates become significant?

But we also consider the more fundamental limitations:

- What if the observed stars are not exactly drawn from the family of model distribution functions?
- What happens to the estimate of the potential and the DF, if the actual potential is not contained in the family of model potentials?

We do not explore the breakdown of the assumption that the system is axisymmetric and in steady state. Except of the test suite on measurement errors in §??, we assume that the phase-space errors are negligible.

REFERENCES

- Batsleer, P., & Dejonghe, H. 1994, *A&A* [TO DO], 287, 43
 Binney, J. 2010, *MNRAS*, 401, 2318
 Binney, J., & McMillan, P. 2011, *MNRAS*, 413, 1889
 Binney, J. 2011, *Pramana*, 77, 39
 Binney, J. 2012, *MNRAS*, 426, 1324
 Binney, J. 2012, *MNRAS*, 426, 1328
 Binney, J. 2013, *NAR* [TO DO: emulateapj doesn't know NAR], 57, 29
 Binney, J., & Tremaine, S. 2008, *Galactic Dynamics: Second Edition*, by James Binney and Scott Tremaine. ISBN 978-0-691-13026-2 (HB). Published by Princeton University Press, Princeton, NJ USA, 2008.
 Bovy, J., & Tremaine, S. 2012, *ApJ*, 756, 89
 [TO DO: In which order should I give the references????] [TO DO: replace the references which I typed myself with the ones from ADS.] [TO DO: Check if all references are actually used in paper. ???]
 Bovy, J., Rix, H.-W., & Hogg, D. W. 2012b, *ApJ*, 751, 131
 Bovy, J., Rix, H.-W., Hogg, D. W. et al., 2012c, *ApJ*, 755, 115
 Bovy, J., Rix, H.-W., Liu, C., et al. 2012, *ApJ*, 753, 148
 Bovy, J., & Rix, H.-W. 2013, *ApJ*, 779, 115
 Bovy, J. 2015, *ApJS*, 216, 29 [TO DO]
 Büdenbender, A., van de Ven, G., & Watkins, L. L. 2015, *MNRAS*, 452, 956
 Dehnen, W. 1998, *AJ*, 115, 2384
 De Lorenzi F., Debattista V.P., Gerhard O., Sambhus N. 2007, *MNRAS*, 376, 7
 Famaey, B., & Dejonghe, H. 2003, *MNRAS*, 340, 752
 Foreman-Mackey, D., Hogg, D. W., Lang, D., & Goodman, J. 2013, *PASP* [TO DO], 125, 306
 Garbari, S., Liu, C., Read, J. I., & Lake, G. 2012, *MNRAS*, 425, 1445
 Henon, M. 1959, *Annales d'Astrophysique*, 22, 126
 Holmberg, J., Nordström, B., & Andersen, J. 2009, *A&A*, 501, 941
 Hunt, J. A. S., & Kawata, D. 2014, *MNRAS*, 443, 2112
 Jurić, M., Ivezić, Ž., Brooks, A., et al. 2008, *ApJ*, 673, 864
 Kawata, D., Hunt, J. A. S., Grand, R. J. J., Pasetto, S., & Cropper, M. 2014, *MNRAS*, 443, 2757
 Klement, R., Fuchs, B., & Rix, H.-W. 2008, *ApJ*, 685, 261
 Kuijken, K., & Gilmore, G. 1989, *MNRAS*, 239, 605
 McMillan, P. 2011, *MNRAS*, 414, 2446
 McMillan, P. J. 2012, *European Physical Journal Web of Conferences*, 19, 10002
 McMillan, P. J., & Binney, J. J. 2008, *MNRAS*, 390, 429
 McMillan, P. J., & Binney, J. 2012, *MNRAS*, 419, 2251
 McMillan, P. J., & Binney, J. J. 2013, *MNRAS*, 433, 1411
 Navarro, J. F., Helmi, A., & Freeman, K. C. 2004, *ApJ*, 601, L43
 Ness, M., Hogg, D. W., Rix, H.-W. et al., 2015, *ApJ*, 808, 16
 Nordström, B., Mayor, M., Andersen, J., et al. 2004, *A&A*, 418, 989
 Perryman, M. A. C., de Boer, K. S., Gilmore, G., et al. 2001, *A&A*, 369, 339
 Piffl, T., Binney, J., McMillan, P. J., et al. 2014, *MNRAS*, 445, 3133
 Read, J. I. 2014, *Journal of Physics G Nuclear Physics*, 41, 063101
 Rix, H.-W., & Bovy, J. 2013, [TO DO] *A&ARv*, 21, 61
 Sackett, P. 1997, *ApJ*, 483, 103
 Sanders, J. L., & Binney, J. 2015, *MNRAS*, 449, 3479
 Sellwood, J. A. 2010, *MNRAS*, 409, 145
 Steinmetz, M. et al., 2006, *AJ*, 132, 1645
 Strigari, L. E. 2013, *Phys. Rep.*, 531, 1
 Syer D., Tremaine S. 1996, *MNRAS*, 282, 223
 Ting, Y.-S., Rix, H.-W., Bovy, J., & van de Ven, G. 2013, *MNRAS*, 434, 652
 Yanny, B., Rockosi, C., Newberg, H. J., et al. 2009, *AJ*, 137, 4377
 Zhang, L., Rix, H.-W., van de Ven, G., et al. 2013, *ApJ*, 772, 108